Inorganic Chemistry

pubs.acs.org/IC Article

Sn(101) Derived from Metal–Organic Frameworks for Efficient Electrocatalytic Reduction of CO_2

Jian-Xiang Wu, Xiao-Rong Zhu, Ting Liang, Xiang-Da Zhang, Shu-Zhen Hou, Ming Xu, Ya-Fei Li,* and Zhi-Yuan Gu*

Cite This: *Inorg. Chem.* 2021, 60, 9653–9659 Read Online

ACCESS | Metrics & More | Article Recommendations | Supporting Information

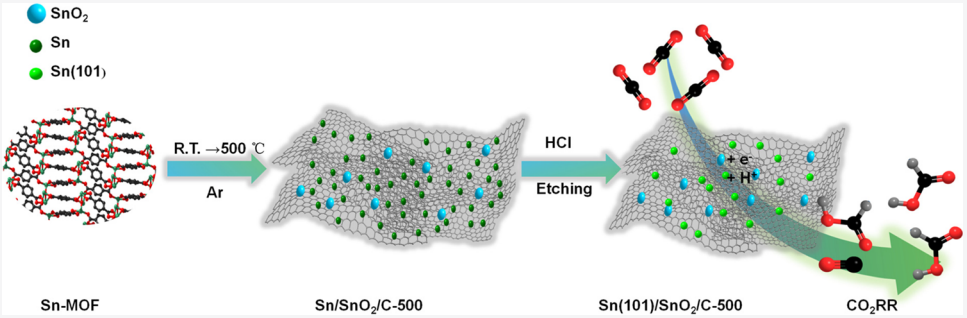

ABSTRACT: The synthesis of a specific Sn plane as an efficient electrocatalyst for CO_2 electrochemical reduction to generate fuels and chemicals is still a huge challenge. Density functional theory (DFT) calculations first reveal that the Sn(101) crystal plane is more advantageous for CO_2 electroreduction. A metal–organic framework (MOF) precursor Sn-MOF has been carbonized and then etched to successfully fabricate Sn(101)/SnO_2/C composites with good control of the carbonization time and the concentration of hydrochloric acid. The Sn(101) crystal plane of the catalyst could enhance the faradaic efficiency of formate to as high as 93.3% and catalytic stability up to 20 h. The promotion of the selectivity and activity by Sn(101) advances new possibilities for the rational design of high-activity Sn catalysts derived from MOFs.

1. INTRODUCTION

It is urgent to design significantly efficient catalysts for CO_2 conversion to generate valuable products due to the increasing amount of CO_2 and massive consumption of fossil fuels.[1−3] Producing carbon-based fuels and chemicals through electrocatalysis of CO_2 (e.g., CO_2RR) has been widely proposed for the storage and utilization of intermittent electricity, which is mainly generated from renewable energy.[4−8] Among the electro-reformed products of CO_2 reduction, the C1 product formate (also known as formic acid, FA) is an important chemical intermediate and can also be stored as a promising chemical fuel for some fuel cells.[9,10] Although it has been reported that In or Pd catalysts could be synthesized to produce FA via electrochemical CO_2RR, most of the metal catalysts generally have poor selectivity for FA due to the high overpotentials and weak affinities toward the $CO_2^{\bullet-}$ intermediate.[11−14] Therefore, it is a technical challenge to develop novel electrocatalysts with high activity, durability, and selectivity for CO_2RR to produce formate.[15−18] Among non-noble metal catalysts, Sn-based catalysts stand out with nontoxicity and low cost.[15,19]

Sn, a cheap and abundant metal, is one of the most attractive catalysts for CO_2RR because of high faradaic efficiency up to 90%.[5,19−24] Different crystal facets usually present different catalytic activities.[25−28] An electrochemical method is developed to produce specific high-index facets.[29,30] However, the synthesis of specific tin crystal facets is rarely explored, although it is significant to CO_2RR and needs further study.

Recently, it has been suggested as an ideal sacrificial template for metal–organic frameworks (MOFs) to fabricate various nanomaterials, including metal/metal-oxide decorated on carbon supports with thermal decomposition at controlled atmospheres.[31−36] Carbon-based nanomaterials, especially single atom catalysts prepared by the novel MOF-templated method, are more effective in electrocatalysis.[36−41] The structural merits result from the uniform distribution of designable metal clusters and organic linkers within the MOF templates. In addition, the thermal decomposition of MOFs can provide the opportunity to form hitherto unrevealed structure catalysts with tailored porosity at the meantime, while diverse treatments with etching reagents offer more effective

Received: March 27, 2021
Published: June 16, 2021

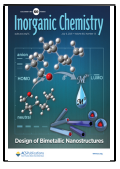

https://doi.org/10.1021/acs.inorgchem.1c00946
Inorg. Chem. 2021, 60, 9653–9659

means to produce specific active sites.[42−49] Nevertheless, Sn-MOF-templated carbon with a specific exposed Sn facet has not yet been explored although it has high potential to selectively produce formate from CO_2RR.

Here, by means of density functional theory (DFT) calculations, we first demonstrate that the Sn(101) crystal plane is energetically more favorable for CO_2RR. Then, we synthesized a series of Sn/SnO_2/C composite catalysts with exposed Sn(101) facets through the carbonization of Sn-MOF ($Sn_3O(1,4\text{-}BDC)_2$) at different temperatures in an argon atmosphere. The high selectivity of electroreduction CO_2 toward formate was obtained and achieved a faradaic efficiency (FE) up to 93.3% using Sn(101)/SnO_2/C-500 (carbonization of Sn-MOF at 500 °C) as the catalyst, where it is higher than most of the reported Sn-based catalysts, such as Sn-MOF, SnO_2, and Sn. The powder X-ray diffraction and catalytic experiments confirmed that the intensity of the Sn(101) diffraction peak is highly relevant to the electrocatalytic activity and selectivity, which could be further enhanced with the optimization of carbonization time and acid etching. These results revealed the fundamental significance of Sn(101) from carbonized Sn-MOF for highly selective production of formate.

2. EXPERIMENTAL METHODS

2.1. Synthesis of Sn-MOF. Zinc sulfate (0.5 mmol) ($SnSO_4$), 0.5 mmol 1,4-benzedicarboyxlic acid, and 1 mmol KOH were added to 10 mL of water and ultrasonicated until fully dissolved Afterward, the mixture was transferred into a Tefion-lined container, which would be put in a steel autoclave, and the reaction temperature was set at 180 °C for 3 days. Water, DMF, and ethanol were used to wash the colorless crystal powder, which dried in a vacuum at 60 °C.[50−52]

2.2. Synthesis of Sn(101)/SnO_2/C-400 and Sn(101)/SnO_2/C-500. The ligands of as-prepared Sn-MOF were removed by pyrolysis in an ultrapure Ar environment at two temperatures (400 and 500 °C) for 2 h with a 5 °C/ min rate for heating. The final obtained products, which were washed with 0.01 mol/L hydrochloric acid and ultrapure water in turn, were dried in the vacuum drying chamber. The samples were denoted as Sn(101)/SnO_2/C-400 and Sn(101)/SnO_2/C-500 according to their pyrolysis temperatures.[53,54]

2.3. Electrochemical Measurement. A typical H-type cell was selected as the electrochemical reactor. With the assistance of an electrochemical workstation, the electrocatalytic data of the working electrode whose surface was coated with the synthesized catalyst could be collected and analyzed.

3. RESULTS AND DISCUSSION

3.1. DFT Calculation. The origin of formate formation with high selectivity observed on the Sn surface was first analyzed by DFT calculations. The simulations were performed on the basis of Sn (101) and (200) planes since they were the predominantly exposed crystal planes. Optimized geometric structures are depicted in Figure 1b,c, while the corresponding energy profiles along the CO_2RR pathway are detailed in Figure 1a. The CO_2RR initiates with a proton-coupled electron transfer to CO_2, leading to the protonation of C or O atoms. Here, we found that the protonation of the O atom to the *COOH is highly endothermic on both (101) and (200) slabs with adsorption free energies of 0.34 and 0.71 eV, respectively. In contrast, the CO_2 activation to *OCHO with the proton added on C atoms proceeds spontaneously thermodynamically. Compared to flat Sn(200) with rather weak *OCHO binding (−0.08 eV), the fold Sn(101) with more exposed top-layer Sn atoms can anchor intermediates more strongly (−0.28 eV), which is more beneficial for the second electron-coupled proton transfer. The

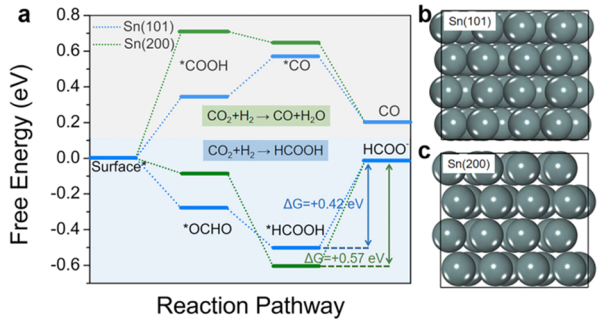

Figure 1. DFT simulation of the CO_2RR process on Sn(101) and Sn(200) planes. (a) Calculated free-energy diagrams for HCOO−, CO formation; optimized geometric structure of (b) Sn(101) and (c) Sn(200).

second H^+/e^- can be added to *OCHO to form *HCOOH with no free-energy barrier to conquer. However, the coordination unsaturated Sn atoms on two planes bind HCOOH strongly, limiting the desorption process potential. A 0.42 V potential is needed to drive the $HCOO^-$ evolution for Sn(101), while another 0.15 V is required for the Sn(200) surface. Therefore, the Sn(101) is a more favorable plane for CO_2RR. The side hydrogen evolution reaction (HER) was also considered. According to our calculations, the adsorption free energies of H* on both Sn(101) (0.23 eV) and Sn(200) (0.51 eV) are much more positive than those of *OCHO, indicating that the side HER can be significantly overwhelmed on the surfaces of Sn. It was worth noting that Sn was more thermodynamically stable at highly reduced working potentials.[15] The p-band center of Sn(101) was much closer to the Fermi-level than that of SnO(101),[55] which indicated the higher CO_2 reduction activities of Sn(101) (Supporting Information Figure S1).

3.2. Synthesis and Characterization of Materials. Inspired by DFT calculations, we successfully synthesized a catalyst with an enhanced Sn(101) plane through Sn-MOF carbonization and acidic etching. Sn-MOF was fabricated by a hydrothermal method and was well characterized (Supporting Information Figures S2-S3).[50−52] The Sn-MOF was then carbonized in a flow of ultrapure argon at 500 °C for 120 min.[53,54] The material was then washed with 0.01 mol/L hydrochloric acid in order to etch Sn and expose the Sn(101) plane. Subsequent characterization showed that the X-ray diffraction (XRD) pattern of the obtained catalyst is well matched with the Sn and SnO_2 mixture (Figure 2a),[19,56,57] while the intensity of the Sn(101) diffraction peak is significantly high possibly due to the selective corrosion of the Sn crystal surface by HCl. The BET surface area was 137.6 m^2/g (Supporting Information Figure S4). For comparison, HCl-etched Sn and SnO_2 and Sn/SnO_2 composites showed no preference in Sn(101), confirming the significance of Sn-MOF in the production of Sn(101) crystal facets (Supporting Information Figure S5). Furthermore, an XRD peak occurred at 2θ = 26.5°, which matched with the graphitic carbon.[34,58] This could also be verified by Raman spectroscopy (Figure 2b); there were clearly two characteristic peaks at 1325 cm^{-1} (D band) and 1588 cm^{-1} (G band). The relative intensity ratio of the D/G band (I_D/I_G) of Sn(101)/SnO_2/C-500 was ∼0.50. Therefore, the material was denoted as Sn(101)/SnO_2/C-500. The further characterization by scanning electron microscopy and high resolution transmission electron microscopy (HRTEM) showed the structural difference between

https://doi.org/10.1021/acs.inorgchem.1c00946
Inorg. Chem. 2021, 60, 9653−9659

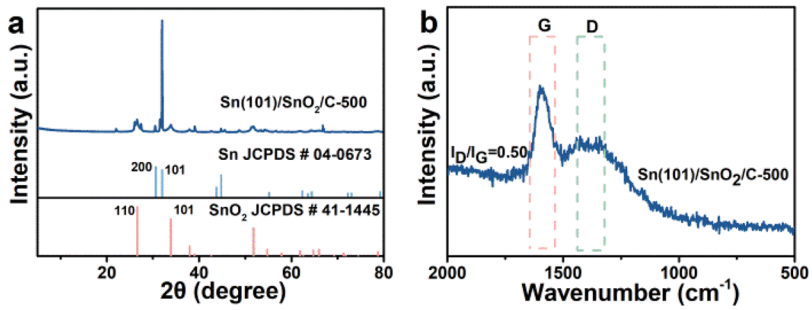

Figure 2. (a) XRD pattern and (b) Raman spectrum of Sn(101)/SnO_2/C-500.

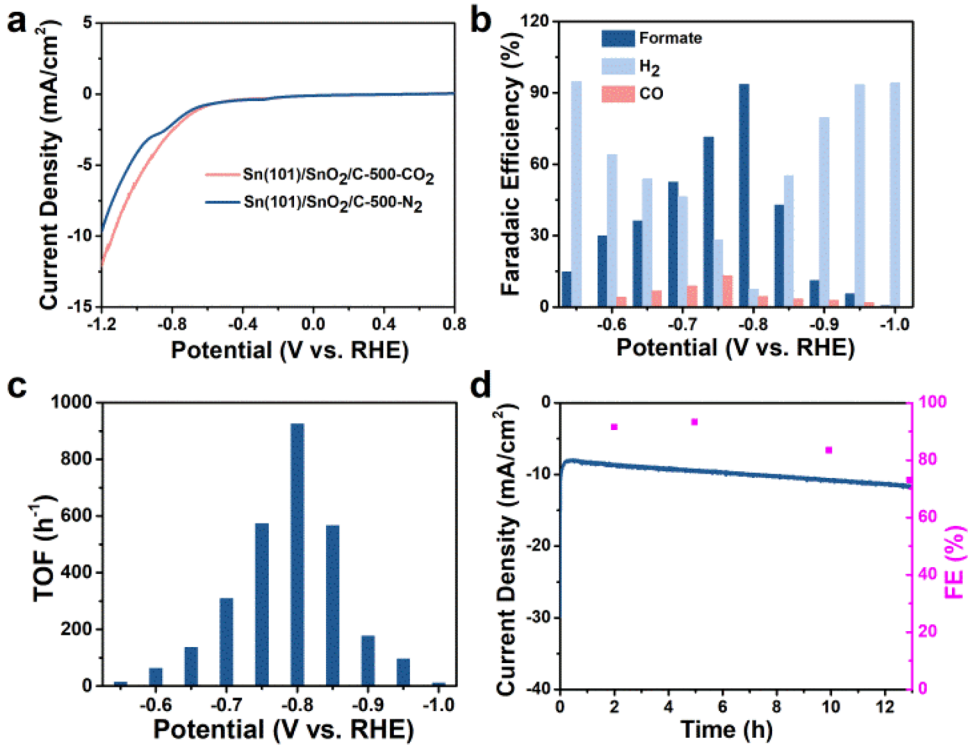

Figure 3. Electrocatalytic property of Sn(101)/SnO_2/C-500: (a) LSV; (b) FE; (c) TOF of formate and (d) long-term stability.

Sn(101)/SnO_2/C-500 and Sn-MOF (see Supplementary Figures S3d, S6a and S6e) and clearly demonstrated Sn(101) lattice fringes (Supporting Information Figure S6f). Due to the structure of Sn-MOF, elemental mapping also revealed the uniform distribution of Sn, C, and O elements in Sn(101)/SnO_2/C-500 (Supporting Information Figure S6b–d). The detailed Sn elemental analysis through X-ray photoelectron spectroscopy elucidated the existence of Sn^{4+}, Sn^{2+}, and Sn^0 with the three split Sn 3d 3/2 peaks (Supporting Information Figure S7a) and the deconvoluted Sn 3d 5/2 signal (Supporting Information Figure S7b).[59] These results suggested that the presence of amorphous SnO is possibly due to surface oxidation of Sn particles,[60] although it could not be identified by XRD.

3.3. Electrochemical Properties. Linear sweep voltammetry (LSV) of Sn(101)/SnO_2/C-500 in CO_2-saturated electrolytes (pH = 7.2) showed a rapid increase of current density from −0.5 V (vs RHE), which was significantly different from that in N_2-saturated (pH = 8.4) (Figure 3a). The electrolysis experiment in N_2 confirmed that the carbon came from CO_2 during CO_2RR in which H_2 was the only product (Supporting Information Figure S8). The electrolysis with Sn(101)/SnO_2/C-500 as the catalyst in CO_2 gave formate and carbon monoxide as major reduction products with a small amount of H_2 from the HER. As shown in Figure 3b and Figure S9, FE of formate was 15.9% at −0.55 V (vs RHE) and then rapidly went up to the maximum of 93.3% at −0.80 V (vs RHE) with a partial current density $j_{formate}$ of 8.2 mA/cm^2. In this condition, TOF was as high as 924 h^{-1} (Figure 3c) with the surface active Sn site of 1.66 × 10^{-7} mol/cm^2 (Supporting Information Figure S10). From −0.55 V to −0.80 V (vs RHE), FE of byproduct CO was very low (FE < 10%), and FE of H_2 was significantly reduced. A further increase of the potential over −0.80 V (vs RHE) could reduce the FE of formate. In addition, the stability of Sn(101)/SnO_2/C-500 could be maintained for 13 h, and its catalytic activity gradually reduced from 93.3 to 72.8% (Figure 3d), which possibly came from the restructuring of the catalyst with the weak Sn(101) crystal plane to form Sn proved by XRD and HRTEM (Supporting Information Figures S11-S12).

3.4. Comparison with Other Sn Catalysts. In order to confirm the effect of Sn(101), we surveyed the CO_2RR activity of conventional Sn-based catalysts, such as Sn, SnO_2, Sn/SnO_2, and Sn-MOF precursors. The experiments suggested that

https://doi.org/10.1021/acs.inorgchem.1c00946
Inorg. Chem. 2021, 60, 9653−9659

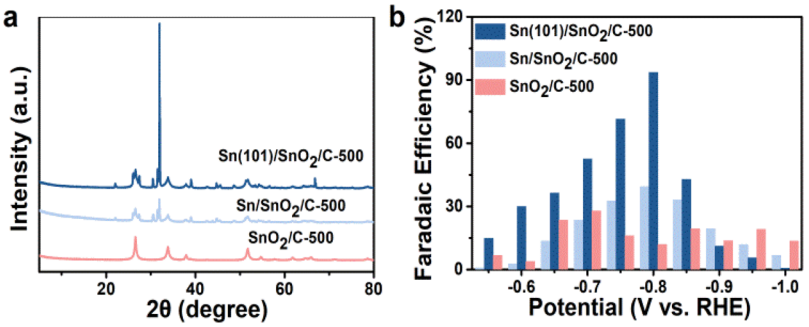

Figure 4. Sn-MOF was carbonized at 500 °C with different hydrochloric acid concentrations for etching (a) XRD and (b) FE of formate.

although CO_2RR was the main cathodic reaction of four catalysts, the selectivity for CO and formate was poor. For Sn, SnO_2, and Sn/SnO_2 catalysts, FE of CO and formate is less than 50%. Meanwhile, for Sn-MOF as the catalyst, FE of formate and CO is up to 61.5 and 21.5%, respectively (Supporting Information Figure S13). Furthermore, the number of active sites of Sn, SnO_2, Sn/SnO_2, and Sn-MOF was lower than that of $Sn(101)/SnO_2/C$-500 (Supporting Information Figure S14). The above results indicated that $Sn(101)/SnO_2/C$-500 could exhibit a much better selectivity for CO_2RR to formate than Sn, SnO_2, Sn/SnO_2, and Sn-MOF.

3.5. Active Center Exploration. To further elucidate the effect of the Sn(101) plane to the selectivity for CO_2RR, the carbonization conditions of Sn-MOF with different times and temperatures were investigated. The catalytic performance and characterization with different carbonization times from 30 min to 120 min were tested without changes of other experimental conditions. The XRD pattern showed that SnO_2 can always be found in the structure (Supporting Information Figure S15b), while the peak of the Sn(101) crystal plane appeared since 60 min and gradually increased gradually on extending the carbonization time. Meanwhile, FE for formate dramatically increased from 45.4 to 93.3% at −0.8 V (vs RHE) with the increase of carbonization time from 30 to 120 min, indicating that the Sn(101) crystal plane indeed enhances the selectivity of formate (Supporting Information Figure S16b). A carbonization temperature of 400 °C with different times from 30 to 120 min was also tested without changes of other experimental conditions, and the catalyst was identified as $Sn(101)/SnO_2/C$-400 through the comprehensive characterization (Supporting Information Figures S15a and S16a). For 120 min (Supporting Information Figures S17−S19), a value as high as 2277 h^{-1} at −0.9 V (vs RHE) (Supporting Information Figure S20c) with the surface active sites of 8.86×10^{-8} mol/cm^2 (Supporting Information Figure S20b) was observed. It was worth noting that the stability of $Sn(101)/SnO_2/C$-400 could be maintained for 20 h with the catalytic activity gradually reduced from 87.6 to 76.8% (Supporting Information Figure S20d). Further optimization of carbonization time at 400 °C also suggested that Sn(101) strongly enhanced the CO_2RR selectivity.

Different etching conditions were the key factors to form Sn(101). We employed no etching and etching with 0.01 and 6 mol/L hydrochloric acid to test the Sn(101) effect on CO_2RR. On the one hand, the material was identified as $Sn/SnO_2/C$-500[53,54] by XRD (Figure 4a and Supporting Information Figure S21a) without etching in which the peaks mainly matched with Sn and SnO_2 without the strong Sn(101) peak. The FE of formate for the catalyst without etching was up to 39.5% (Figure 4b and Supporting Information Figure S22b) at −0.80 V (vs RHE), indicating the poor formate selectivity. On the other hand, with 6 mol/L hydrochloric acid etching, the Sn component was removed throughout to generate SnO_2/C-500, confirmed by XRD (Figure 4a and Supporting Information Figure S21b). The SnO_2/C-500 catalyst was poor for formate between −0.55 and −1.0 V (vs RHE) with the highest FE of only 27.9% (Figure 4b and Supporting Information Figure S23b). With appropriate etching conditions (0.01 mol/L), the obtained $Sn(101)/SnO_2/C$-500 showed superior CO_2RR performance to the above two materials. A similar correlation between etching conditions and catalytic activity with a carbonization temperature of 400 °C was also observed (Supporting Information Figures S21, S22a and S23a), strongly demonstrating that the etching was crucial for the Sn(101) crystal plane to efficiently produce formate.

4. CONCLUSIONS

In summary, Sn(101) was a more favorable plane for CO_2RR revealed by both DFT calculations and experimental evidence. Therefore, a Sn(101)-containing catalyst was successfully fabricated with the precise control of carbonization and etching conditions, which efficiently catalyzed CO_2 to formate with FE of 93.3% and TOF of 924 h^{-1}. This work would open up a new opportunity for the synthesis of specific oriented crystal planes from presynthesized MOFs, which could further promote the real application of electrocatalytic CO_2RR.

■ ASSOCIATED CONTENT

Supporting Information

The Supporting Information is available free of charge at https://pubs.acs.org/doi/10.1021/acs.inorgchem.1c00946.

Experimental details, synthesis of materials, electrochemical measurements, materials characterization, electrocatalytic performance, and calculation methods (PDF)

■ AUTHOR INFORMATION

Corresponding Authors

Ya-Fei Li − *Jiangsu Key Laboratory of Biofunctional Materials, Jiangsu Collaborative Innovation Center of Biomedical Functional Materials, Jiangsu Key Laboratory of New Power Batteries, School of Chemistry and Materials Science, Nanjing Normal University, Nanjing, Jiangsu 210023, P. R. China;* orcid.org/0000-0003-2587-820X; Email: liyafei@njnu.edu.cn

Zhi-Yuan Gu − *Jiangsu Key Laboratory of Biofunctional Materials, Jiangsu Collaborative Innovation Center of*

https://doi.org/10.1021/acs.inorgchem.1c00946
Inorg. Chem. 2021, 60, 9653−9659

Biomedical Functional Materials, Jiangsu Key Laboratory of New Power Batteries, School of Chemistry and Materials Science, Nanjing Normal University, Nanjing, Jiangsu 210023, P. R. China; orcid.org/0000-0002-6245-4759; Email: guzhiyuan@njnu.edu.cn

Authors

Jian-Xiang Wu − *Jiangsu Key Laboratory of Biofunctional Materials, Jiangsu Collaborative Innovation Center of Biomedical Functional Materials, Jiangsu Key Laboratory of New Power Batteries, School of Chemistry and Materials Science, Nanjing Normal University, Nanjing, Jiangsu 210023, P. R. China*

Xiao-Rong Zhu − *Jiangsu Key Laboratory of Biofunctional Materials, Jiangsu Collaborative Innovation Center of Biomedical Functional Materials, Jiangsu Key Laboratory of New Power Batteries, School of Chemistry and Materials Science, Nanjing Normal University, Nanjing, Jiangsu 210023, P. R. China*

Ting Liang − *Orthopaedic Institute, Medical College, Soochow University, Suzhou, Jiangsu 215006, P. R. China*

Xiang-Da Zhang − *Jiangsu Key Laboratory of Biofunctional Materials, Jiangsu Collaborative Innovation Center of Biomedical Functional Materials, Jiangsu Key Laboratory of New Power Batteries, School of Chemistry and Materials Science, Nanjing Normal University, Nanjing, Jiangsu 210023, P. R. China*

Shu-Zhen Hou − *Jiangsu Key Laboratory of Biofunctional Materials, Jiangsu Collaborative Innovation Center of Biomedical Functional Materials, Jiangsu Key Laboratory of New Power Batteries, School of Chemistry and Materials Science, Nanjing Normal University, Nanjing, Jiangsu 210023, P. R. China*

Ming Xu − *Jiangsu Key Laboratory of Biofunctional Materials, Jiangsu Collaborative Innovation Center of Biomedical Functional Materials, Jiangsu Key Laboratory of New Power Batteries, School of Chemistry and Materials Science, Nanjing Normal University, Nanjing, Jiangsu 210023, P. R. China*

Complete contact information is available at: https://pubs.acs.org/10.1021/acs.inorgchem.1c00946

Author Contributions

Z.-Y.G. and Y.-F.L. supervised the project. J.-X.W. and T.L. contributed to the design of experiments and the analysis of collected data. X.-R.Z. carried out the corresponding theoretical calculation. X.-D.Z., S.-Z.H., and M.X. redound to the additional experimental details and relevant characterizations. This manuscript was mainly written by J.-X.W., X.-R.Z., and Z.-Y.G. All authors assisted with the manuscript discussions and checks. J.W., X.-R.Z., and T.L. contributed equally to this work.

Notes

The authors declare no competing financial interest.

■ ACKNOWLEDGMENTS

This work was financially supported from the National Natural Science Foundation of China (No. 21922407), the Natural Science Foundation of Jiangsu Province of China (No. BK20190086), the Priority Academic Program Development of Jiangsu Higher Education Institutions, and the Fellowship of China Postdoctoral Science Foundation (No. 2020 M681149).

■ REFERENCES

(1) Gao, S.; Lin, Y.; Jiao, X.; Sun, Y.; Luo, Q.; Zhang, W.; Li, D.; Yang, J.; Xie, Y. Partially oxidized atomic cobalt layers for carbon dioxide electroreduction to liquid fuel. *Nature* **2016**, *529*, 68.

(2) Takeda, H.; Ohashi, K.; Sekine, A.; Ishitani, O. Photocatalytic CO_2 reduction using Cu (I) photosensitizers with a Fe (II) catalyst. *J. Am. Chem. Soc.* **2016**, *138*, 4354−4357.

(3) He, Q.; Liu, D.; Lee, J. H.; Liu, Y.; Xie, Z.; Hwang, S.; Kattel, S.; Song, L.; Chen, J. G. Electrochemical Conversion of CO_2 to Syngas with Controllable CO/H_2 Ratios over Co and Ni Single-Atom Catalysts. *Angew. Chem. Int. Ed.* **2020**, *59*, 3033−3037.

(4) Zhang, Y.; Zhang, X.; Ling, Y.; Li, F.; Bond, A. M.; Zhang, J. Controllable Synthesis of Few-Layer Bismuth Subcarbonate by Electrochemical Exfoliation for Enhanced CO_2 Reduction Performance. *Angew. Chem. Int. Ed.* **2018**, *57*, 13283−13287.

(5) Zhang, S.; Kang, P.; Meyer, T. J. Nanostructured Tin Catalysts for Selective Electrochemical Reduction of Carbon Dioxide to Formate. *J. Am. Chem. Soc.* **2014**, *136*, 1734−1737.

(6) Zhu, D. D.; Liu, J. L.; Qiao, S. Z. Recent advances in inorganic heterogeneous electrocatalysts for reduction of carbon dioxide. *Adv. Mater.* **2016**, *28*, 3423−3452.

(7) de Jesus Gálvez-Vázquez, M.; Moreno-García, P.; Xu, H.; Hou, Y.; Hu, H.; Montiel, I. Z.; Rudnev, A. V.; Alinejad, S.; Grozovski, V.; Wiley, B. J.; Arenz, M.; Broekmann, P. Environment Matters: CO_2RR Electrocatalyst Performance Testing in a Gas-Fed Zero-Gap Electrolyzer. *ACS Catal.* **2020**, *10*, 13096−13108.

(8) Pan, F.; Li, B.; Sarnello, E.; Hwang, S.; Gang, Y.; Feng, X.; Xiang, X.; Adli, N. M.; Li, T.; Su, D.; Wu, G.; Wang, G.; Li, Y. Boosting CO_2 reduction on Fe-N-C with sulfur incorporation: Synergistic electronic and structural engineering. *Nano Energy* **2020**, *68*, No. 104384.

(9) Agarwal, A. S.; Zhai, Y.; Hill, D.; Sridhar, N. The electrochemical reduction of carbon dioxide to formate/formic acid: engineering and economic feasibility. *ChemSusChem* **2011**, *4*, 1301−1310.

(10) Enthaler, S.; von Langermann, J.; Schmidt, T. Carbon dioxide and formic acid—the couple for environmental-friendly hydrogen storage? *Energ. Environ. Sci.* **2010**, *3*, 1207−1217.

(11) Hori, Y.; Kikuchi, K.; Suzuki, S. Production of CO and CH_4 in Electrochemical Reduction of CO_2 at Metal Electrodes in Aqueous Hydrogencarbonate Solution. *Chem. Lett.* **1985**, *14*, 1695−1698.

(12) Hori, Y.; Wakebe, H.; Tsukamoto, T.; Koga, O. Electrocatalytic process of CO selectivity in electrochemical reduction of CO_2 at metal electrodes in aqueous media. *Electrochim. Acta* **1994**, *39*, 1833−1839.

(13) Hori, Y. I. *Electrochemical CO2 reduction on metal electrodes. In Modern aspects of electrochemistry*; Springer, 2008; 89−189.

(14) Pan, F.; Yang, Y. Designing CO_2 reduction electrode materials by morphology and interface engineering. *Energ. Environ. Sci.* **2020**, *13*, 2275−2309.

(15) Han, N.; Wang, Y.; Yang, H.; Deng, J.; Wu, J.; Li, Y.; Li, Y. Ultrathin bismuth nanosheets from in situ topotactic transformation for selective electrocatalytic CO_2 reduction to formate. *Nat. Commun.* **2018**, *9*, 1320.

(16) Chen, Z.; Mou, K.; Wang, X.; Liu, L. Nitrogen-Doped Graphene Quantum Dots Enhance the Activity of Bi2O3 Nanosheets for Electrochemical Reduction of CO_2 in a Wide Negative Potential Region. *Angew. Chem. Int. Ed.* **2018**, *57*, 12790−12794.

(17) Bai, X.; Chen, W.; Zhao, C.; Li, S.; Song, Y.; Ge, R.; Wei, W.; Sun, Y. Exclusive Formation of Formic Acid from CO_2 Electroreduction by a Tunable Pd-Sn Alloy. *Angew. Chem. Int. Ed.* **2017**, *56*, 12219−12223.

(18) Fan, K.; Jia, Y.; Ji, Y.; Kuang, P.; Zhu, B.; Liu, X.; Yu, J. Curved Surface Boosts Electrochemical CO_2 Reduction to Formate via Bismuth Nanotubes in a Wide Potential Window. *ACS Catal.* **2020**, *10*, 358−364.

(19) Li, F.; Chen, L.; Knowles, G. P.; MacFarlane, D. R.; Zhang, J. Hierarchical mesoporous SnO_2 nanosheets on carbon cloth: a robust and flexible electrocatalyst for CO_2 reduction with high efficiency and selectivity. *Angew. Chem. Int. Ed.* **2017**, *56*, 505−509.

(20) Chen, Y.; Kanan, M. W. Tin Oxide Dependence of the CO_2 Reduction Efficiency on Tin Electrodes and Enhanced Activity for Tin/Tin Oxide Thin-Film Catalysts. *J. Am. Chem. Soc.* **2012**, *134*, 1986−1989.
(21) Li, Q.; Fu, J.; Zhu, W.; Chen, Z.; Shen, B.; Wu, L.; Xi, Z.; Wang, T.; Lu, G.; Zhu, J.-j. Tuning Sn-catalysis for electrochemical reduction of CO_2 to CO via the core/shell Cu/SnO_2 structure. *J. Am. Chem. Soc.* **2017**, *139*, 4290−4293.
(22) Ye, K.; Zhou, Z.; Shao, J.; Lin, L.; Gao, D.; Ta, N.; Si, R.; Wang, G.; Bao, X. In Situ Reconstruction of a Hierarchical Sn-Cu/SnO_x Core/Shell Catalyst for High-Performance CO_2 Electroreduction. *Angew. Chem. Int. Ed.* **2020**, *59*, 4814−4821.
(23) Zheng, X.; Ji, Y.; Tang, J.; Wang, J.; Liu, B.; Steinrück, H.-G.; Lim, K.; Li, Y.; Toney, M. F.; Chan, K. Theory-guided Sn/Cu alloying for efficient CO_2 electroreduction at low overpotentials. *Nat. Catal.* **2019**, *2*, 55−61.
(24) Lim, J.; Kang, P. W.; Jeon, S. S.; Lee, H. Electrochemically deposited Sn catalysts with dense tips on a gas diffusion electrode for electrochemical CO_2 reduction. *J. Mater. Chem. A* **2020**, *8*, 9032−9038.
(25) Roy, N.; Sohn, Y.; Pradhan, D. Synergy of low-energy {101} and high-energy {001} TiO_2 crystal facets for enhanced photocatalysis. *ACS Nano* **2013**, *7*, 2532−2540.
(26) Sun, H.; Ruess, R.; Schlettwein, D.; Yoshida, T. Influence of Crystal Facets (102) or (100) on Photoelectrochemical Kinetics of ZnO Nanocrystals in Dye-Sensitized Solar Cells. *J. Electrochem. Soc.* **2019**, *166*, B3290−B3294.
(27) Huang, L.; Zhang, X.; Han, Y.; Wang, Q.; Fang, Y.; Dong, S. High-index facets bounded platinum−lead concave nanocubes with enhanced electrocatalytic properties. *Chem. Mater.* **2017**, *29*, 4557−4562.
(28) Rabiee, H.; Zhang, X.; Ge, L.; Hu, S.; Li, M.; Smart, S.; Zhu, Z.; Yuan, Z. Tuning the Product Selectivity of the Cu Hollow Fiber Gas Diffusion Electrode for Efficient CO_2 Reduction to Formate by Controlled Surface Sn Electrodeposition. *ACS Appl.Mater. Inter.* **2020**, *12*, 21670−21681.
(29) Swetha, P.; Feng, S.-P. High-index facet defined shape-controlled electrochemical synthesis of nanocrystals: A mini review. *Electrochem. Commun.* **2018**, *94*, 64−69.
(30) Cho, F.-H.; Lin, Y.-C.; Lai, Y.-H. Electrochemically fabricated gold dendrites with high-index facets for use as surface-enhanced Raman-scattering-active substrates. *Appl. Surf. Sci.* **2017**, *402*, 147−153.
(31) Zhou, X.; Tian, J.; Hu, J.; Li, C. High Rate Magnesium−Sulfur Battery with Improved Cyclability Based on Metal−Organic Framework Derivative Carbon Host. *Adv. Mater.* **2018**, *30*, No. 1704166.
(32) Guan, B. Y.; Lu, Y.; Wang, Y.; Wu, M.; Lou, X. W. Porous Iron−Cobalt Alloy/Nitrogen-Doped Carbon Cages Synthesized via Pyrolysis of Complex Metal−Organic Framework Hybrids for Oxygen Reduction. *Adv. Funct. Mater.* **2018**, *28*, No. 1706738.
(33) Yang, W.; Li, X.; Li, Y.; Zhu, R.; Pang, H. Applications of Metal−Organic-Framework-Derived Carbon Materials. *Adv. Mater.* **2018**, *31*, No. 1804740.
(34) Zhu, Q. L.; Xia, W.; Akita, T.; Zou, R.; Xu, Q. Metal-Organic Framework-Derived Honeycomb-Like Open Porous Nanostructures as Precious-Metal-Free Catalysts for Highly Efficient Oxygen Electroreduction. *Adv. Mater.* **2016**, *28*, 6391−6398.
(35) Yang, S. J.; Nam, S.; Kim, T.; Im, J. H.; Jung, H.; Kang, J. H.; Wi, S.; Park, B.; Park, C. R. Preparation and exceptional lithium anodic performance of porous carbon-coated ZnO quantum dots derived from a metal−organic framework. *J. Am. Chem. Soc.* **2013**, *135*, 7394−7397.
(36) Ma, T. Y.; Dai, S.; Jaroniec, M.; Qiao, S. Z. Metal−organic framework derived hybrid Co_3O_4-carbon porous nanowire arrays as reversible oxygen evolution electrodes. *J. Am. Chem. Soc.* **2014**, *136*, 13925−13931.
(37) Chaikittisilp, W.; Torad, N. L.; Li, C.; Imura, M.; Suzuki, N.; Ishihara, S.; Ariga, K.; Yamauchi, Y. Synthesis of Nanoporous Carbon−Cobalt-Oxide Hybrid Electrocatalysts by Thermal Conversion of Metal−Organic Frameworks. *Chem-Eur. J.* **2014**, *20*, 4217−4221.
(38) Hou, Y.; Huang, T.; Wen, Z.; Mao, S.; Cui, S.; Chen, J. Metal−organic framework-derived nitrogen-doped core-shell-structured porous Fe/Fe_3C@ C nanoboxes supported on graphene sheets for efficient oxygen reduction reactions. *Adv. Energy Mater.* **2014**, *4*, No. 1400337.
(39) Zhang, Y.; Jiao, L.; Yang, W.; Xie, C.; Jiang, H.-L. Rational Fabrication of Low-Coordinate Single-Atom Ni Electrocatalysts by MOFs for Highly Selective CO_2 Reduction. *Angew. Chem. Int. Ed.* **2021**, *60*, 7607−7611.
(40) Gong, Y.-N.; Jiao, L.; Qian, Y.; Pan, C.-Y.; Zheng, L.; Cai, X.; Liu, B.; Yu, S.-H.; Jiang, H.-L. Regulating the Coordination Environment of MOF-Templated Single-Atom Nickel Electrocatalysts for Boosting CO_2 Reduction. *Angew. Chem. Int. Ed.* **2020**, *59*, 2705−2709.
(41) Jiao, L.; Yang, W.; Wan, G.; Zhang, R.; Zheng, X.; Zhou, H.; Yu, S.-H.; Jiang, H.-L. Single-Atom Electrocatalysts from Multivariate Metal−Organic Frameworks for Highly Selective Reduction of CO_2 at Low Pressures. *Angew. Chem. Int. Ed.* **2020**, *59*, 20589−20595.
(42) Aijaz, A.; Fujiwara, N.; Xu, Q. From metal−organic framework to nitrogen-decorated nanoporous carbons: high CO_2 uptake and efficient catalytic oxygen reduction. *J. Am. Chem. Soc.* **2014**, *136*, 6790−6793.
(43) Zhao, D.; Shui, J. L.; Grabstanowicz, L. R.; Chen, C.; Commet, S. M.; Xu, T.; Lu, J.; Liu, D. J. Highly Efficient Non-Precious Metal Electrocatalysts Prepared from One-Pot Synthesized Zeolitic Imidazolate Frameworks. *Adv. Mater.* **2014**, *26*, 1093−1097.
(44) Zhang, P.; Sun, F.; Xiang, Z.; Shen, Z.; Yun, J.; Cao, D. ZIF-derived in situ nitrogen-doped porous carbons as efficient metal-free electrocatalysts for oxygen reduction reaction. *Energ. Environ. Sci.* **2014**, *7*, 442−450.
(45) Zhang, W.; Wu, Z.-Y.; Jiang, H.-L.; Yu, S.-H. Nanowire-directed templating synthesis of metal−organic framework nanofibers and their derived porous doped carbon nanofibers for enhanced electrocatalysis. *J. Am. Chem. Soc.* **2014**, *136*, 14385−14388.
(46) Zhong, H. X.; Wang, J.; Zhang, Y. W.; Xu, W. L.; Xing, W.; Xu, D.; Zhang, Y. F.; Zhang, X. B. ZIF-8 derived graphene-based nitrogen-doped porous carbon sheets as highly efficient and durable oxygen reduction electrocatalysts. *Angew. Chem. Int. Ed.* **2014**, *53*, 14235−14239.
(47) Xia, W.; Zou, R.; An, L.; Xia, D.; Guo, S. A metal−organic framework route to in situ encapsulation of Co@Co_3O_4@Ccore@ bishell nanoparticles into a highly ordered porous carbon matrix for oxygen reduction. *Energ. Environ. Sci.* **2015**, *8*, 568−576.
(48) Wu, J.-X.; Hou, S.-Z.; Zhang, X.-D.; Xu, M.; Yang, H.-F.; Cao, P.-S.; Gu, Z.-Y. Cathodized copper porphyrin metal−organic framework nanosheets for selective formate and acetate production from CO_2 electroreduction. *Chem. Sci.* **2019**, *10*, 2199−2205.
(49) Wu, J.-X.; Yuan, W.-W.; Xu, M.; Gu, Z.-Y. Ultrathin 2D nickel zeolitic imidazolate framework nanosheets for electrocatalytic reduction of CO_2. *Chem. Commun.* **2019**, *55*, 11634−11637.
(50) Wang, X.; Liu, L.; Makarenko, T.; Jacobson, A. J. Acentric and Centric Interpenetrations of an Anionic Framework Mediated by Cation Sizes: The Alkali-Metal Tin (II) Benzenedicarboxylates $A_2Sn_2(bdc)_3(H_2O)_x$ (A= Li, Na, K, Rb, Cs). *Cryst. Growth Des.* **2010**, *10*, 1960−1965.
(51) Wang, X.; Liu, L.; Makarenko, T.; Jacobson, A. J. Influence of ligand geometry on the dimensionality of Sn (II) benzenedicarboxylate crystal structures. *Cryst. Growth Des.* **2010**, *10*, 3752−3756.
(52) Wu, N.; Wang, W.; Kou, L. Q.; Zhang, X.; Shi, Y. R.; Li, T. H.; Li, F.; Zhou, J. M.; Wei, Y. Enhanced Li Storage Stability Induced by Locating Sn in Metal−Organic Frameworks. *Chem-Eur. J.* **2018**, *24*, 6330−6333.
(53) Shiva, K.; Jayaramulu, K.; Rajendra, H.; Kumar Maji, T.; Bhattacharyya, A. J. In-situ Stabilization of Tin Nanoparticles in Porous Carbon Matrix derived from Metal Organic Framework: High Capacity and High Rate Capability Anodes for Lithium-ion Batteries. *Z. Anorg. Allg. Chem.* **2014**, *640*, 1115−1118.

https://doi.org/10.1021/acs.inorgchem.1c00946
Inorg. Chem. 2021, 60, 9653−9659

(54) Zhou, X.; Chen, S.; Yang, J.; Bai, T.; Ren, Y.; Tian, H. Metal−organic frameworks derived okra-like SnO_2 encapsulated in nitrogen-doped graphene for lithium ion battery. *ACS Appl. Mater. Interfaces* **2017**, *9*, 14309−14318.
(55) Wang, S.; Wang, J.; Xin, H. Insights into electrochemical CO_2 reduction on tin oxides from first-principles calculations. *Green Energy Environ.* **2017**, *2*, 168−171.
(56) Zhang, Y.; Chen, L.; Li, F.; Easton, C. D.; Li, J.; Bond, A. M.; Zhang, J. Direct detection of electron transfer reactions underpinning the tin-catalyzed electrochemical reduction of CO_2 using Fourier-transformed ac voltammetry. *ACS Catal.* **2017**, *7*, 4846−4853.
(57) Yang, J.; Chen, S.; Tang, J.; Tian, H.; Bai, T.; Zhou, X. Rod-like hierarchical Sn/SnO_x@ C nanostructures with enhanced lithium storage properties. *Appl. Surf. Sci.* **2018**, *435*, 203−209.
(58) Chen, Y. Z.; Wang, C.; Wu, Z. Y.; Xiong, Y.; Xu, Q.; Yu, S. H.; Jiang, H. L. From bimetallic metal-organic framework to porous carbon: high surface area and multicomponent active dopants for excellent electrocatalysis. *Adv. Mater.* **2015**, *27*, 5010−5016.
(59) An, X.; Li, S.; Yoshida, A.; Wang, Z.; Hao, X.; Abudula, A.; Guan, G. Electrodeposition of Tin-Based Electrocatalysts with Different Surface Tin Species Distributions for Electrochemical Reduction of CO_2 to HCOOH. *ACS Sustainable Chem. Eng.* **2019**, *7*, 9360−9368.
(60) Hoflund, G. B.; Corallo, G. R. Electron-energy-loss study of the oxidation of polycrystalline tin. *Phys. Rev. B* **1992**, *46*, No. 7110.

https://doi.org/10.1021/acs.inorgchem.1c00946
Inorg. Chem. 2021, 60, 9653−9659